HOKKAIDO UNIVERSITY

Title	Improving Oxygen Evolution Reaction Performance and Durability Using Rhombic Dodecahedral PtNiIr Nanoframes with Metal Oxide Supports in Acidic Media
Author(s)	Tadgell, Colin A; Kato, Masaru; Miyabayashi, Keiko et al.
Citation	ACS Catalysis, 13(18), 12288-12298 https://doi.org/10.1021/acscatal.3c02541
Issue Date	2023-09-05
Doc URL	https://hdl.handle.net/2115/93041
Rights	This document is the Accepted Manuscript version of a Published Work that appeared in final form in ACS Catalysis, copyright © American Chemical Society after peer review and technical editing by the publisher. To access the final edited and published work see https://pubs.acs.org/articlesonrequest/AOR-D6UGHHES9KTF9RMB2PRN.
Type	journal article
File Information	NF_ATO_revised-manuscript_ver03.pdf

Hokkaido University Collection of Scholarly and Academic Papers : HUSCAP

Improving Oxygen Evolution Reaction Performance and Durability Using Rhombic Dodecahedral PtNiIr Nanoframes with Metal Oxide Supports in Acidic Media

Colin A. Tadgell,[*,†] Masaru Kato,[*,†] Keiko Miyabayashi,[‡] Ichizo Yagi[*,†]

[†] *Faculty of Environmental Earth Science, Hokkaido University, N10W5, Kita-ku, Sapporo 060-0810, Japan*
[‡] *Graduate School of Integrated Science and Technology, Shizuoka University, 3-5-1, Naka-ku, Hamamatsu, Shizuoka, 432-8561, Japan*
KEYWORDS: Oxygen Evolution Reaction, Electrocatalyst, Antimony-doped Tin Oxide, Platinum-Iridium Alloys, Nanoframe.

ABSTRACT: Carbon corrosion is a common problem during the oxygen evolution reaction (OER) in water electrolysis which occurs at high anodic potentials. Metal oxides can be used to improve overall durability and activity *via* catalyst/support interactions in the OER, but many of these oxides suffer from low electrical conductivity. Recently, antimony-doped tin oxide (ATO) has been shown to offer sufficient conductivity and low dissolution in acidic environments. Here, PtNiIr nanoframes (NFs) were successfully loaded onto ATO using a *n*-butylamine treatment and tested under OER conditions. These PtNiIr NFs form a rhombic dodecahedral shape with Pt and Ir forming a homogenous alloy at the edges and vertices. The PtNiIr NF/ATO electrocatalyst shows comparable results to PtNiIr NF/C with current densities of 0.57 and 0.62 mA/cm^2 at 1.53 V_{RHE}. The Faradaic efficiency for the OER of PtNiIr NF/ATO was found to be 92% which was close to NF/C at 94%. Furthermore, PtNiIr NF/ATO shows a lower dissolution during accelerated durability testing which was further shown during online electrochemical mass spectrometry measurements. PtNiIr NF/ATO showed only a minor decrease in mass activity (0.57 to 0.54 A/mg based on PGM content) at 1.53 V_{RHE} after 10,000 potential cycles and no signs of dissolution or catalyst migration when compared to PtNiIr NF/C.

1. Introduction

The generation of hydrogen as a fuel is vital in maintaining a sustainable hydrogen economy.[1] Presently, the production of hydrogen is facilitated through the use of water electrolysis via alkaline electrochemical methods. However, the implementation of proton exchange membrane water electrolyzers (PEMWEs) provides a high operation current density, energy efficiency, and ease of operation. Current limitations of PEMWEs include higher cost and loading of an anodic electrocatalyst, which is often iridium or ruthenium based.[1-2] Therefore, a method of reducing platinum group metal (PGM) content while retaining catalytic activity and durability is paramount. Modification of catalyst composition (alloying, doping, etc.), size, shape, and the support material provides promising materials systems to improve the oxygen evolution reaction (OER) occurring within PEMWEs.

Alloying of platinum with 3d transition elements have been widely reported as a method of improving catalyst activity as well as reducing platinum content and improving durability.[3-5] For instance, the Pt_3Ni catalyst has demonstrated notable enhancements in mass activity as well as continued performance in oxygen reduction reaction applications over 10,000 potential cycles.[5-8] By altering the catalyst shape, the overall surface geometry and electronic structure can also be optimized. Pt_3Ni rhombic dodecahedral nanoframes (NFs) provide Pt-skin surfaces and atoms with low coordination numbers on their edges and vertexes. These low coordination number atoms have been shown a higher catalytic activity in comparison to higher coordination atoms in the bulk.[9] Adoption of the rhombic dodecahedral shape has continued with the implementation of binary and ternary alloy additions, PtNiRh NFs in the ethanol oxidation reaction, PtCuRh NFs in the methanol oxidation reaction, or IrNi NFs in OER applications.[10-12] Excess surface nickel can be chemically removed via chemical or electrochemical methods with the benefit of exposing more platinum, or iridium, atoms to the surface.[3-5]

OER catalysts are commonly loaded onto carbon-based supports (mesoporous, graphene, carbon nanotubes, etc.) as another method to lower the amount of noble metal used.[13-15] Carbon porous transport layers are commonly used in PEMWEs which undergo harsh operating conditions.[13] Initiating the OER in PEMWEs requires operating potentials higher than 1.4 V vs. RHE and can reach potentials more positive than 2.0 V vs. RHE.[13-15] This imposes limitations on carbon-based supports due to observable carbon oxidation at potentials increasing positively above 1.0 V vs. RHE which limits usage in commercial systems.[13]

Due to the high anodic potentials applied during the OER, conventional carbon-based supports are susceptible to corrosion and are often replaced by metal oxide and carbide supports (TiO_x, TiC, SnO_2, etc.).[15-22] Of these metal oxide candidates, antimony-doped tin oxide (ATO) is considered one

of the most promising candidates for the OER in acidic media.[23] These metal oxide systems require a sufficient conductivity to be viable, in addition to showing a high degree of stability. The immobilization of iridium oxide nanoparticles on ATO showed the OER activity comparable or even surpassing an iridium black reference.[24] Iridium exhibited a synergistic reaction with ATO which was attributed to strong metal support interactions (SMSIs).

SMSIs promote charge transfer across the interface between the metal nanoparticle and the metal oxide. Spillover, or reverse spillover, involves the activation of a reactant on one surface to another and can occur at this interface as well, where SnO_2 has been shown to provide OH groups in the removal of intermediate CO_{ads} improving ethanol oxidation reaction performance.[10] Briux *et al*. observed reverse spillover of oxygen from the oxide surface to platinum in a Pt/CeO_2 catalyst which may induce spontaneous dissociation of O-H bonds in water and lead to a 20-fold improvement in catalytic activity in comparison with Pt(111).[4,25] More recent studies using *operando* near-ambient pressure X-ray photoelectron spectroscopy (XPS) of iridium supported and unsupported ATO reported a decrease in binding energy of Sn $3d_{5/2}$ with potential and a significantly lower rate of oxidation of Ir/ATO, where oxygen atom spillover occurs from Ir to ATO.[26] Furthermore, Oh *et al*. reported a 8-fold increase in kinetic water splitting activity of iridium nanodendrites supported on ATO owing to improved charge transfer interactions.[2] Analyzing Pt, Ir catalysts in XPS showed that an excessive presence of platinum in PtNiIr NFs resulted in reduction of overall iridium active sites and demonstrated the importance of Ir^{III} sites in lowering the kinetic barriers to the O-O bond formation necessary for improving OER activity.[27-28]

Herein, we propose a method for loading highly active PtNiIr NFs onto ATO supports (PtNiIr NF/ATO) using a n-butylamine-based treatment.[7] PtNiIr NF/ATO shows comparable OER activity with PtNiIr NFs loaded onto a carbon support (PtNiIr NF/C). Several loading processes were attempted for comparison to find the most effective way to load NFs onto ATO nanoparticles. Following loading, samples were electrochemically tested in 0.1 M $HClO_4$ using linear sweep voltammetry and the OER was monitored using online electrochemical mass spectrometry (OLEMS).[29] Accelerated durability testing (ADT) was done and samples were examined before and after ADT using XPS and inductively coupled plasma mass spectrometry (ICP-MS).

2. Experimental Section

Materials. Hexane, 2-propanol, perchloric acid, oleylamine, n-butylamine, acetic acid, toluene, $Ni(NO_3)_2{\cdot}6H_2O$, and 5% Nafion DE520 were purchased from Wako Pure Chemical Industries, Ltd. Ethanol was acquired from Japan Alcohol Trading Co. Ltd. $H_2PtCl_6{\cdot}6H_2O$ was purchased from Tanaka Kikinzoku Kogyo. $IrCl_3$ was obtained from Sigma Aldrich Chemical Companies. Iridium black (99.9%) was acquired from Strem Chemicals Inc. ATO (30 wt% in a methyl isobutyl ketone/isobutanol solution) was provided by Dai Nippon Toryo Co., Ltd.

Preparation of PtNi and PtNiIr rhombic dodecahedral NFs. PtNi and PtNiIr NFs were prepared in two steps via the preparation of rhombic dodecahedral nanocrystals from a modified synthetic procedure in the literature.[5,7-8] For the preparation of PtNi rhombic dodecahedral nanocrystals, $H_2PtCl_6{\cdot}6H_2O$ (100 mg, 0.193 mmol), $Ni(NO_3)_2{\cdot}6H_2O$ (64.3 mg, 0.221 mmol), and oleylamine (20 mL) were mixed in a two-necked flask (100 mL). The reaction mixture was mixed for 30 min. at 353 K in air and then heated in an aluminum block heater at 553 K under argon for ca. 10 min until the mixture turned black and then was further heated for 4 min. The flask was placed in an ice bath for ca. 2 min to quench the reaction. The PtNiIr rhombic dodecahedral nanocrystals were synthesized using the above-mentioned method with the addition of $IrCl_3$ (68.8 mg, 0.229 mmol) into the reaction mixture prior to heating. Rhombic dodecahedral nanocrystals were isolated from the reaction mixture at 10,000 rpm for 10 min. using Micro Refrigerated Centrifuge 3700 equipped with an angle rotor AF-5004CA (Kubota Co.) for seven cycles rinsing with an ethanol and hexane mixture (ca. 20 mL, 1:1 *v*/*v*) between each cycle. Yield: ca. 10 mg.

The rhombic dodecahedral nanocrystals were dispersed in a mixture of oleylamine (1 mL), acetic acid (20 mL), toluene (20 mL) in an eggplant-shaped flask (100 mL) and were refluxed in an oil bath for 2 h at 363 K under air. Following acid corrosion, the sample was immersed in a similar ethanol/hexane mixture and isolated by centrifugation at 10,000 rpm for 10 min at least seven times to obtain the resultant nanoframes. The obtained NFs were kept in ethanol in a dark location at room temperature to prevent agglomeration. Yield ca. 7 mg.

Preparation of PtNi and PtNiIr NF/C. To create carbon-supported samples, Vulcan XC-72R (0.7 mg) was dispersed in ethanol and sonicated in an ice bath for 30 min. PtNi and PtNiIr NFs (0.3 mg) were added to the solution at 30 wt% loading for another 30 min with continued sonication in the ice bath. Following sonication, the mixture was removed of solvent at 373 K and then dried in a furnace at 473 K overnight. Yield: ca. 1.0 mg. The metal content of 30wt% of the catalyst was confirmed by inductively coupled plasma mass spectrometry (ICP-MS).

Preparation of PtNiIr NF/ATO. The commercial ATO solution (0.025 mL) containing methyl isobutyl ketone/isobutanol was separated by immersion in ethanol (10 mL) and centrifugation at 10,000 rpm for 10 min at least 3 times. Ethanol, ethylene glycol, or *n*-butylamine (10 mL) was then added, and the mixture was sonicated for 30 min. PtNiIr NFs were introduced at 30 wt% loading to the ATO. The dispersion was stirred at 300 rpm at room temperature for three days. The product was isolated from the reaction mixture and rinsed with the ethanol and hexane mixture (ca. 20 mL, 1:1 v/v) under centrifugation at 10,000 rpm for 10 min. for at least 8 times to obtain PtNiIr NF/ATO. Yield: ca. 1.5 mg. The metal content of the catalyst was confirmed by ICP-MS before electrochemical testing.

Electrochemical measurements. Electrochemical measurements were performed using a conventional three-electrode setup. A potentiostat (HZ-7000, Hokuto Denko) was used to record cyclic voltammograms (CVs) and linear sweep voltammograms (LSVs). A disk electrode including the catalyst-modified glassy carbon (GC) screw was used as the working electrode. An Ag|AgCl (sat. KCl) electrode with a double junction holder (International chemistry Co., Ltd) and platinum foil were used as the reference and the counter electrodes, respectively.

A GC screw (5 mm φ, M4, Tokai Carbon Co., Ltd.) was polished with alumina polishing slurry (0.3 μm, Baikalox), followed by a finer polishing slurry (0.05 μm, Baikalox) for two min each prior to sonication in acetone and then Milli-Q water for at least 5 min in each solvent. Catalyst ink was prepared using 0.70 mg of each catalyst (PtNiIr NF/C, PtNi NF/C, PtNiIr NF/ATO, PtNi NF/ATO and iridium black) was dispersed in the mixture of 0.30 mL of 2-propanol, 0.95 mL of Milli-Q water and 5.0 μL of 5% Nafion DE520 in ice–water under ultrasonication for two hours. The catalyst ink (15 μL) was drop-cast on the GC disk that was rotating at 700 rpm using an AFMSRX Analytical Rotator and a MSRX Speed Controller (PINE Re-

search Instrumentation) and then dried at room temperature. Platinum loading on the GC disk was 18.3 μg/cm² for all catalyst samples.

CVs and LSVs were recorded in an aqueous solution containing 0.1 M $HClO_4$ under argon. The electrolyte solution was purged with argon for at least 30 min before electrochemical measurements. An *iR* correction was applied to all OER polarization curves to accommodate ohmic resistance.

For CO stripping voltammetry measurements, 0.1 M $HClO_4$ aqueous electrolyte solution was purged with CO for 5 min and then with Ar for 60 min. A bias potential of 0.05 V vs. RHE was applied to a sample electrode during purging with CO and Ar until CO stripping voltammetry measurements had begun. CVs and LSVs were recorded in the potential range from 0.05 to 1.45 V vs. RHE for two cycles. Electrochemically active surface areas based on electrochemical oxidation of CO charges ($ECSA_{CO}$) and hydrogen desorption charges ($ECSA_{Hupd}$) were determined from the difference between the first and second cycles.

ADT was performed for 10,000 cycles between 1.2 and 1.6 V vs. RHE at a sweep rate of 100 mV s^{-1} in an Ar-saturated 0.1 M $HClO_4$ aqueous solution. OER polarization curves were recorded before and after ADT in the range of 1.0 to 1.8 V_{RHE} (prior to *iR* correction) under argon. The turnover frequency (TOF) was calculated from these results according to Equation 1:

$$\mathrm{TOF} = \frac{j_{1.53V} \cdot A_{GC}}{n_e \cdot F \cdot n_{Pt+Ir}} \quad (1)$$

where $j_{1.53V}$ is the current density for the OER at the *iR*-corrected 1.53 V vs. RHE, A_{GC} denotes the geometrical surface area of the GC electrode, F is the Faraday constant (96485.3 C mol^{-1}), n_e represents the number of transferred electrons per molecule of oxygen (n_e = 4) and n_{Pt+Ir} is the total number of moles of noble metals on the electrode determined by ICP-MS. It was assumed that all noble metal content was available for the oxygen evolution reaction.

Physicochemical measurements. XPS data were collected at a pass energy of 10 eV using an Al X-ray source on a photoelectron spectrometer JPS-9200 (JEOL). The C=C peak value in the C1s region was used as the internal standard (284.6 eV). Catalyst ink was drop-cast onto a glassy carbon plate (ca. 1 x 1 cm^2) at 343 K and placed in a vacuum to dry overnight. ICP–MS was performed using an ICP–MS spectrometer 8800 ICP-QQQ (Agilent Technologies). For sample preparation, catalyst ink was dried and then the dispersion in aqua regia was stirred at 308 K for 24 h. The dispersion was filtered through a membrane filter (13HP045AN, ADVANTEC), and then the filtrate was diluted with Milli-Q water. Scanning transmission electron microscopy (STEM) images were taken at an acceleration voltage of 200 kV using HD-2000 (Hitachi Scientific Instrument). High angle annular dark-field scanning transmission electron microscopy (HAADF–STEM) and energy dispersive spectroscopy (EDS) elemental mapping images were taken using a JEOL JEM-ARM200F instrument at 200 kV.

OLEMS Measurements. An OLEMS setup was used as previously reported in the literature.[29] The OLEMS setup consists of a quadrupole mass spectrometer (M201QA-TDM, CANON ANELVA), metal ionization gauge (GI-M2, ULVAC), a rotary vane vacuum pump (GLD-135, ULVAC) and a turbo molecular vacuum pump (5150 Turbo Pump, Alcatel) equipped with a controller (CFF450, Alcatel). A glass pinhole provided an inlet for gas. A thin GORE PTFE membrane (VE91221, 0.32 mm in thickness) and a POREFLON membrane (HP-010-30; pore size: 0.1 μm; thickness: 30 μm) were placed over the pinhole prior to heating from a heat gun. The inner diameter of the pinhole was below 10 μm. All connections were tightly sealed, and no leakage was detected during the measurement. The glassy carbon working electrode was immersed in 0.1 M $HClO_4$ solution purged with argon and was placed within 30 μm of the pinhole detector. The internal pressure was 3-4 $\times 10^{-4}$ Pa during the OLEMS experiments. The OLEMS equipment was calibrated using pure oxygen mixed with argon at different flow rates to create a calibration curve, shown in **Figure** S1.

Product analysis for OER. All measurements in the OLEMS setup was conducted in an electrochemical cell similar to previous work and containing 0.1 M $HClO_4$ under argon for at least 30 min before electrochemical measurements.[29] An Ag|AgCl (sat. KCl) electrode with a double junction holder (International chemistry Co., Ltd) and platinum foil were used as the reference and the counter electrodes, respectively. Catalyst-modified GC was used as the working electrode. All LSVs in positive going sweep under Ar are corrected through the subtraction of current densities of the working electrode. LSVs were recorded at a sweep rate of 5 mV s^{-1} from 1.0 and 1.8 V_{RHE} under Ar. Formation of volatile products (m/z = 2, 16, 18, 28, 30, 32, 34, 36, 44) was monitored using OLEMS.

Faradaic efficiency of O_2 (m/z = 32) was quantified using a calibration constant (S^*) which was obtained from currents at potentiostat and OLEMS as reported in recent work.[27,30,31] Chronopotentiometric measurements were applied at 2 mA cm^{-2} for 300 s. Calculating the integrated areas from galvanostat and mass spectrometric ion currents led to galvanostatic and mass spectrometric charges, respectively. The calibration constant was determined using the ion current from both OLEMS ($i_{ms,j}$) and current measured from the electrode (i_F), as shown in Equation 2. This calibration constant is used to determine the Faradaic efficiency in Equation 3.[27,31]

$$S^* = \frac{i_{\mathrm{ms}} \cdot z}{i_{\mathrm{F}}} \quad (2)$$

$$FE\ (\%) = \frac{Q_{\mathrm{ms}} \cdot z}{Q_{\mathrm{F}} \cdot S^*} \quad (3)$$

where z is the number of transferred electrons per molecule of oxygen (z = 4), the values from integrating the current with respect to the time potential was applied from both the mass spectrometric ion current from OLEMS (Q_{ms}) and the Faradaic current from the working electrode (Q_F), and S^* is a constant obtained from the calibration data in **Figure** S1. For each sample, three independent OLEMS measurements were done with the Faradaic efficiency discussed being the average value presented with error bars. OER measurements in the OLEMS setup were not *iR* corrected.

The S-number is a measure of the amount of oxygen evolved per iridium atom dissolved during the OER and was determined from chronopotentiometric measurements at 5 mA cm^{-2} for 1000 s in the OLEMS setup.[32] Drop-cast catalyst ink was dried following testing and dispersed in ethanol before dissolution in aqua regia. The S-number was determined from Equation 4 as outlined in other studies.[27,31,32]

$$\mathrm{S-Number} = \frac{\eta_{O_2}}{\eta_{\mathrm{Ir,\,dissolved}}} \quad (4)$$

The value of η_{O2} is determined stoichiometrically from the charge of electrons measured from OLEMS. The value of η_{Ir} is found from the number of iridium atoms dissolved after electrochemical measurements by ICP-MS. Both values were converted to mols of O_2 and $Ir_{dissolved}$.

X-ray absorption spectroscopy (XAS) measurement. Ir L_{III}-edge XAS measurements were performed at the beamline 12C, Photon Factory (PF), KEK, Japan. The data were collected at room temperature using a Zn foil (μt = 6) as a filter for a 7-element silicon drift detector (SDD) in the fluorescence mode. Iridium black was used as a reference material for calibrating the beamline in the fluorescence mode. Catalyst inks of PtNiIr NF/C, PtNiIr NF/ATO and iridium black were dropcast onto carbon paper (Perma foil PF-20UHP, Toyo Tanso) and were firmly attached to a three-electrode spectroelectrochemical flow cell[33] ensuring that a tight seal was maintained. 0.1 M $HClO_4$ (purged for 30 min. in N_2) was flowed into the cell interior which also contained a Pt-wire counter electrode and a no-leak Ag|AgCl (3 M KCl) reference electrode. Each sample underwent electrochemical cleaning before XAS measurements using an Ivium Compactstat potentiostat. *In situ* XAS measurements were conducted at open circuit potential. X-ray absorption near-edge structure (XANES) spectra were normalized using Athena software.[34]

3. Results and Discussion

PtNiIr NFs were prepared in two steps: preparation of PtNiIr rhombic dodecahedral nanocrystals in the first step and chemical corrosion of the synthesized rhombic dodecahedral nanocrystals in the second step.[5,7] NF synthesis consisted of heating an oleylamine solution containing $H_2PtCl_6{\cdot}6H_2O$, $IrCl_3$ and $Ni(NO_3)_2{\cdot}6H_2O$ at 553 K under Ar gave rhombic dodecahedron nanocrystals. STEM-EDS images in **Figure** 1a-e show an ordered, alloyed lattice at the edges and vertices where the lattice spacing was found to coincide with the (111) lattice projection, determined from **Figure** 1f. Increasing the synthesis time was found to produce a tetradecapod structure in a Pt-rich shell similar to the previous work, shown in **Figure** S2.[7]

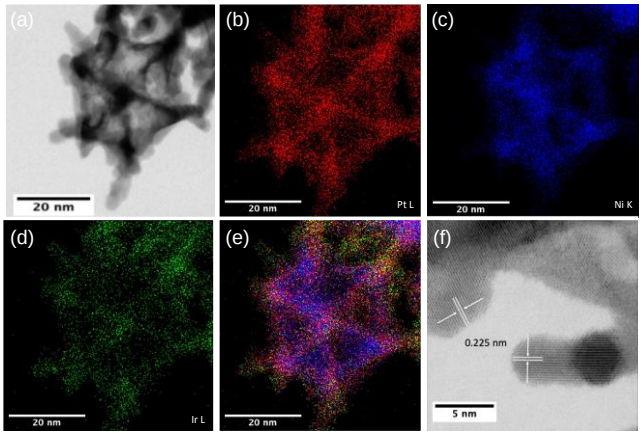

Figure 1. (a) STEM image of PtNiIr NFs. (b-e) EDS mapping images (blue: Ni; red: Pt; and green: Ir). (f) STEM image of a Pt-Ir edge with lattice spacing.

These PtNiIr NFs were then immobilized onto ATO using *n*-butylamine ($BuNH_2$): PtNiIr NFs and ATO were added to $BuNH_2$ and stirred for three days at room temperature. STEM images of PtNiIr NF/ATO and PtNiIr NF/C are shown in **Figure** 2a and 2b, respectively. An even distribution of nanoframes was noted on both supports.

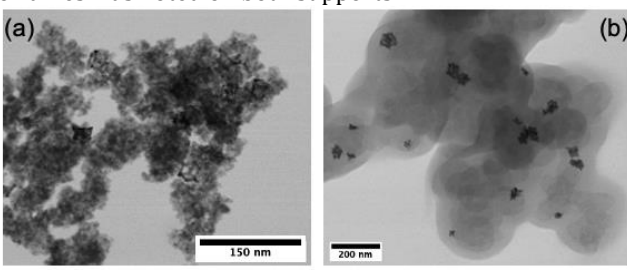

Figure 2. STEM images of PtNiIr NFs loaded onto: (a) commercial ATO and (b) Vulcan XC-72R carbon supports.

Use of $BuNH_2$ was also found to improve OER performance of PtNiIr/ATO samples when examining the loading when NFs were immersed in $BuNH_2$ or ethylene glycol. This was confirmed by comparing LSVs for the OER in 0.1 M $HClO_4$ aq. under Ar (see **Figure** S3a). PtNiIr NF/ATO loaded in different solvents showed an increasing OER response when $BuNH_2$ was used compared to loading in ethylene glycol shown in **Figure** S3a. After electrochemical cleaning, the LSV for the $BuNH_2$ loading method provided a current density of 1.02 mA/cm^2 at 1.53 V_{RHE}. Pt_3Ni NFs are contrasted with this data to demonstrate the lower OER activity as well as for comparison in the CV shown in **Figure** S3b.[7]

The use of $BuNH_2$ was found to be more effective for loading PtNiIr NFs onto ATO than that of ethylene glycol or ethanol. Oleylamine remains on the nanoframe surface even following acid treatment and still required a heat treatment step.[37] $BuNH_2$ can be used to replace long-chain alkyl amine of oleylamine on NF surfaces via a ligand exchange reaction.[38-42] Although ethylene glycol can also be used for loading IrO_x nanoparticles onto ATO,[24,35-36] it was not effective for the NF loading onto ATO in this work. Arán-Ais *et al.* demonstrated that a mixture of methanol and NaOH is effective to remove oleylamine from the surface of nanomaterials but ethanol is not.[43] The balance of hydrophobicity and basicity of cleaning solvents seems to be critical to remove oleylamine. $BuNH_2$ is also helpful to disperse ATO in solution compared with ethylene glycol: the isoelectric point of ATO powder is reported to be pH_{iep} = 3.7 [44] and therefore negatively charged ATO can be more stabilized in $BuNH_2$ than ethylene glycol. $BuNH_2$ was found to increase the dispersibility of ATO in solution, resulting in the successful loading of PtNiIr NFs onto ATO.

Further supporting evidence can be seen in the improvement of PtNiIr NFs distribution across the loaded supports, shown in **Figures** S4, S5 and S6. Prior to $BuNH_2$ treatment, NF density remains similar but the amount of agglomeration is much higher. Examining the catalyst performance with and without acid corrosion shows a clear benefit to the dissolution of the Ni-rich core prior to loading.

Using $BuNH_2$-assisted loading, PtNiIr NF/ATO was tested and contrasted with iridium black and PtNiIr NF/C. Prior to OER measurements, the catalysts were treated using electrochemical cleaning in Ar-saturated 0.1M $HClO_4$ between 0.05 and 1.5 V vs. RHE for 50 cycles at a sweep rate of 500 mV/s. This electrochemical cleaning treatment has been demonstrated in previous studies to remove excess surface nickel remaining after synthesis and acid corrosion.[5,7] PtNi nanoframes were loaded in a similar fashion to PtNiIr nanoframes onto carbon and ATO supports. Additionally, commercial iridium black was tested as a reference material for the OER.

Figure 3 a-c compares LSVs of PtNi NF/C, PtNi NF/ATO, PtNiIr NF/C, PtNiIr NF/ATO and iridium black for the OER. PtNiIr NF/C and NF/ATO showed more negative onset potentials for the OER than iridium black. The mass activity based on the PGM content at 1.53 V_{RHE} for PtNiIr NF/C (0.62 A/mg) was slightly higher than that of PtNiIr NF/ATO (0.57 A/mg). In contrast, iridium black was found to have a mass activity of 0.069 A/mg, which was comparable to previous report (0.048-0.066 A/mg).[24,27,45]

Using Electrochemically active surface areas from electrochemical CO oxidation charges ($ECSA_{CO}$), the specific activity was determined to be 4.26 and 6.01 A/m^2 for PtNiIr NF/C and PtNiIr NF/ATO respectively. They are higher than that of iridium black (0.784 A/m^2). PtNi NF/C, in the absence of iridium, showed mass activities around 0.03 A/mg. The leaching of nickel from the PtNiIr structure leads to the formation of an amorphous IrO_x structure eroded from IrNi alloy core/edges which provides much higher catalytic activities on both supports.[27,46,47] Without these defects, a much lower mass activity would be expected due to a mostly metallic Ir edge.[28] For PtNiIr NF/C and PtNiIr NF/ATO catalysts overpotential values at 10 mA/cm^2 were

found to be 287 and 316 mV, respectively.[48] The excellent range of overpotentials measured at 10 mA/cm^2 noted in the study by Tahir *et al*. was between 300 and 400 mV.[48]

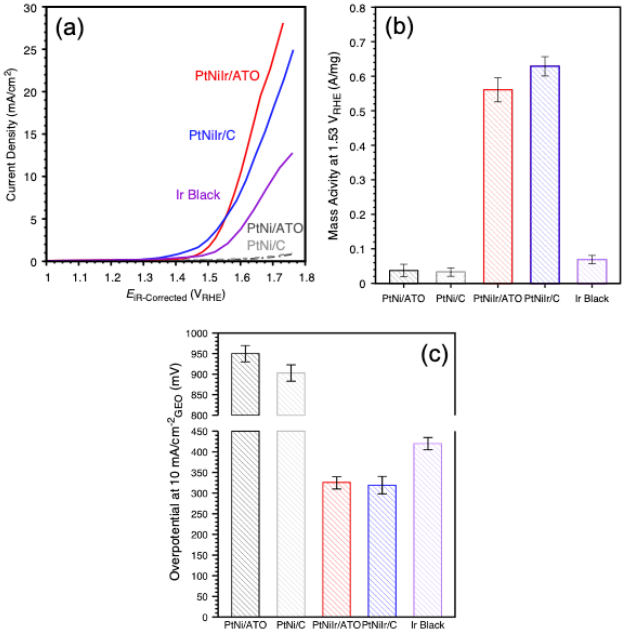

Figure 3. Comparing PtNiIr NFs supported on ATO and carbon with iridium black: (a) OER polarization curves at a sweep rate of 5 mV/s between 1.0 and 1.8 V_{RHE} in 0.1 M $HClO_4$ solution (b) mass activities at 1.53 V_{RHE} and (c) measured overpotentials at 10 mA/cm^2

Electrochemically active surface areas were calculated from electrochemical CO oxidation charges ($ECSA_{CO}$) and charges of desorption of underpotentially deposited hydrogen ($ECSA_{Hupd}$), see **Figure** S7. $ECSA_{CO}$ for both PtNiIr NF/C and PtNiIr NF/ATO were found to be 75.3 and 49.6 m^2 g^{-1} based on PGM content, respectively. The ratio of $ECSA_{CO}/ECSA_{H\text{-}upd}$ gives indication if a Pt-skin has formed when the value is greater than one. The ratio of $ECSA_{CO}/ECSA_{H\text{-}upd}$ for PtNi NF/C was found to be 1.22, which was in agreement with previous studies.[7] In contrast, the ratio for PtNiIr NF/ATO was found to be 1.10, suggesting that the iridium is present at the surface and increases the CO adsorption energy as noted in other studies.[3,49]

Turnover frequencies (TOFs), Faradaic efficiencies and *S*-numbers were determined by OLEMS. The TOFs in **Figure** S8 represent the catalytic activity of a particular unit site on the catalysts and allow comparison between the carbon and ATO supports. The TOFs at 1.53V_{RHE} of PtNiIr NF/C and NF/ATO were found to be similar, 0.31 and 0.30 s^{-1} respectively. This result is more than 10 times that of the reference iridium black at 0.036 s^{-1}. **Figure** S8c shows the Faradaic efficiency at 2 mA/cm^2 over 300 s for PtNiIr NF/C and PtNiIr NF/ATO was determined to be 93.9% and 92.2% respectively. The Faradaic efficiency of iridium black was found to be 88.3%. The values were reasonable when compared to other studies.[27,36]

The stability of the catalyst support can also be examined from the *S*-number which has been used previously as a metric for overall durability in OER.[32] This was calculated from potentiostatic electrochemical measurements at 5 mA/cm^2 over 1000 s. The calculated *S*-numbers are shown in **Figure** S8d. PtNiIr NF/ATO showed the highest value of 5.5 ± 0.2 ×10^4, which suggests that this electrocatalyst shows a lower amount of iridium dissolution during the OER. This is reflected in the values of iridium loss observed in ICP-MS results (**Table** S1). The *S*-number of iridium black was found to be close to previous published works demonstrating the measurements validity.[27]

XPS measurements were conducted to examine the electronic state of surface platinum on ATO as a support. The results are shown in **Figure** 4a and b. Lewera *et al*. examined SMSI using XPS measurements of platinum supported on carbon, tungsten oxide and titanium oxide.[50] They observed a shoulder on the higher binding energy side of Pt $4f_{7/2}$ and $4f_{5/2}$ peaks of carbon supports resulting from a higher level of oxidation of Pt. This shoulder is observed in PtNiIr NF/C in **Figure** 4b around 77 eV (on the grey original data); however, no shoulder was seen in PtNiIr NF/ATO (**Figure** 4a). ATO has been shown to correlate to improved catalytic performance.[50] Values of Pt^0 $4f_{7/2}$ were found at a lower binding energy for PtNiIr NF/ATO compared to PtNiIr NF/C (70.47 and 71.06 eV, respectively) and the peaks appear more asymmetric indicating a lower degree of oxidation for Pt as observed by Oh *et al*.[36] This can be induced by the SMSI, which shifts the d-band center of Pt to the Fermi level.[49,50] Reduced catalyst surface oxides, such as metal alloy catalysts loaded on ATO, have been shown to correlate to improved catalytic performance.[50]

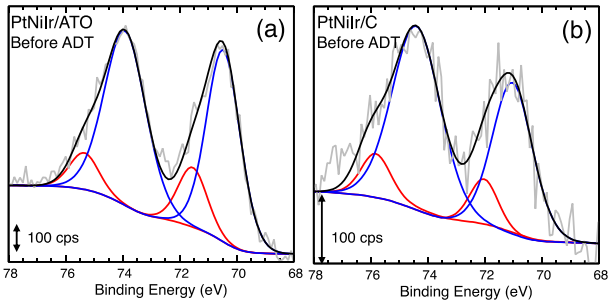

Figure 4. XPS data of (a) PtNiIr NF/ATO and (b) PtNiIr NF/C in the Pt 4f region after electrochemical activation. The lines in grey show the original measured spectra, the black line shows the data envelop and the blue and red lines show the deconvolution of Pt^0 and Pt^{II} states for each sample.

Ir L_{III}-edge XANES spectra of iridium black, PtNiIr NF/C, and PtNiIr NF/ATO, in 0.1 M $HClO_4$ under N_2, following electrochemical cleaning/activation are shown in **Figure** 5. White line peak positions in Ir L_{III}-edge XANES region are sensitive to changes in the oxidation state of Ir because the white line peak ($2p_{3/2}$→ 5d transition) intensity reflects the degree of the vacancy of Ir 5d orbitals near the Fermi level.[36] Such that higher intensities indicate higher oxidation states of Ir. Examining white line positions of each peak following activation, the absorption at 11,215 and 11218.5 eV corresponds to the $2p_{3/2}$ to 5d electronic transition of Ir and IrO_2, respectively.[36]

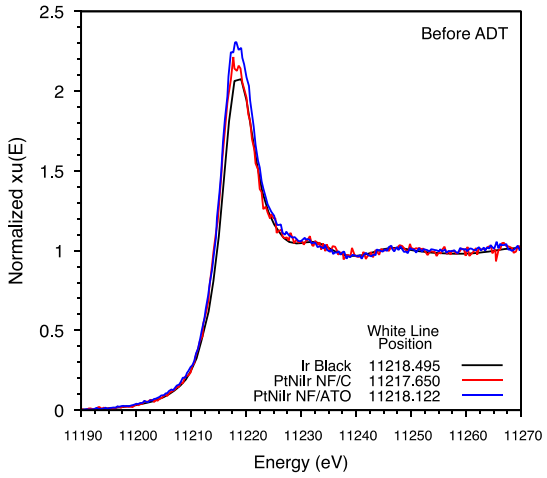

Figure 5. XANES data at the Ir L_{III} edge showing iridium black as well as PtNiIr NF/ATO and PtNiIr NF/C following electrochemical activation in 0.1 M $HClO_4$.

From the XANES spectra (**Figure** 5), iridium black has been oxidized to IrO_2 by the electrochemical cleaning/activation process and has an oxidation state of Ir^{IV}. In addition, PtNiIr NF/ATO and PtNiIr NF/C are located at a slightly lower energy indicating that predominantly Ir^{IV} is present, which is in agreement with previous XANES analysis of Ir and ATO.[27,36] Strasser *et al*. noted that Ir-O values had shifted to higher values when compared to IrO_x on carbon support or crystalline IrO_2 which indicated a lower oxidation state of iridium on metal oxide supports.[36,51] IrO_x nanoparticles in these studies would have a higher degree of contact than PtNiIr NFs such that more iridium can interact with the metal oxide. However, a higher white line intensity was observed for PtNiIr NF/ATO indicates a greater amount of IrO_2 than PtNiIr NF/C. The change in intensity can indicate a change between environment and Ir 5d orbitals, signifying a charge donation between iridium and the support.[52,53] The higher white line intensity in PtNiIr NF/ATO demonstrates an increase in charge donation from the NFs to the support when compared to PtNiIr NF/C. This would imply stronger metal support interactions following electrochemical cleaning. In addition, the amount of platinum present in the NFs has an impact on the amount of iridium active sites and the degree of oxidation.[27] **Table** S1 reveals that a larger degree of nickel dissolution occurs on the carbon supports which leads to a larger presence of platinum with surface iridium.

ADT was conducted at 10,000 cycles between 1.2 and 1.6 V_{RHE} under argon at a sweep rate of 100 mV/s. CO stripping peaks were shifted before and after ADT (**Figure** S9). The peak potential of CO stripping voltammograms are sensitive to the surface composition and are directly correlated with shifts in the Pt d-band center.[50] In this study, the shift was found to be -0.05 V for PtNiIr NF/C which is close to shifts observed in previous work on PtNi NF/C (–0.1 V).[7,8] The shift for PtNiIr NF/ATO was found to be -0.03 V and comparable to that of PtNiIr NF/C. From XPS studies of the Pt 4f region and XAS studies of the Ir L_{III} edge, a general trend of platinum reduction, and iridium oxidation is observed, respectively. Thus, a trend of charge transfer from platinum to iridium is likely occurring leading to oxygen moving to iridium surface sites. This would reinforce the work observed by Choi *et al.* where iridium lowers the kinetic barrier to O-O formation which improves the overall OER activity.[27] This seems to be further improved with interaction of these oxidized iridium surface sites and the metal support interactions of ATO.

LSVs for PtNiIr NF/ATO, PtNiIr NF/C and iridium black are shown in **Figure** 6 a-c before and after ADT. PtNiIr NF/ATO showed almost no loss in OER activity after ADT. There is a minor decrease in the mass activity at 1.53 V vs. RHE from 0.57 to 0.54 A/mg based on PGM content, determined by ICP-MS. In contrast, PtNiIr NF/C showed a sharp decrease in the OER performance following ADT: the overall mass activity decreases from 0.62 to 0.42 A/mg. In contrast, pure iridium black lost more than half of its initial mass activity (0.025 A/mg). The losses in metal content before and after ADT were found to be quite comparable with a decrease in nickel from the PtNiIr NFs of 15 at% leading to an increase in surface Pt with only minor losses in Ir of 0.5 at% (shown in **Table** S1). **Figure** 6d compares the results of ADT of 10,000 cycles and demonstrates the increased durability found for PtNiIr NFs loaded onto ATO.

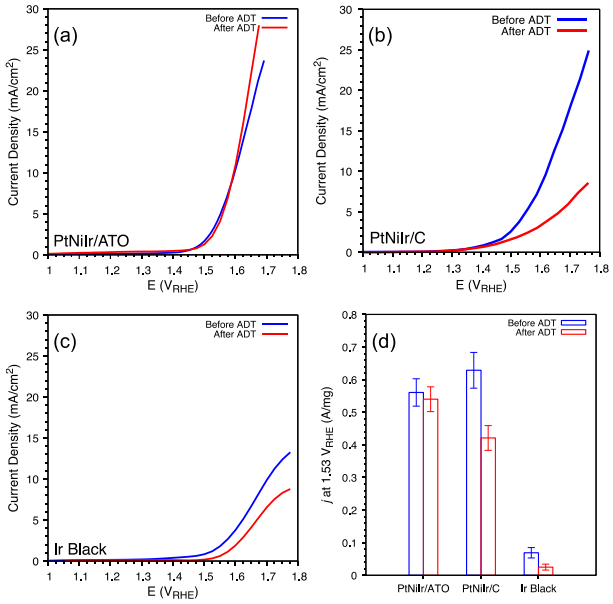

Figure 6. Before and ADTs for 10,000 cycles for: (a) PtNiIr NF/ATO (b) PtNiIr NF/C (c) iridium black and (d) comparative current densities for each sample before (traces in blue) and after (traces in red) ADT.

STEM images of PtNiIr NF/C after ADT for 10,000 cycles showed signs of carbon corrosion, nanoframe detachment, and migration across the surface (**Figure** 7a and b). A much higher degree of carbon corrosion, where carbon in the presence of water reacts to form carbon dioxide, leads to the removal of support and the migration of PtNiIr NFs. Qualitatively, a lower distribution of NFs was observed for PtNiIr NF/C samples and some areas of the carbon support appeared amorphous as noted in previous literature.[13-14] The interaction between platinum and carbon has been shown to lower the onset potential of the carbon corrosion reaction and the weak bonding with platinum leads to detachment, dissolution, and agglomeration. Indeed, after ADT, less NFs were visible on the carbon support surface and agglomeration/dissolution of NFs was observed as shown in **Figure** 7b. A single solitary NF is shown next to an amorphous carbon surface in **Figure** 7a. In contrast, PtNiIr NFs

loaded onto ATO remain well distributed, showing no signs of migration or dissolution, and there is no indication of dissolution of the support structure (**Figure** 7c and d).

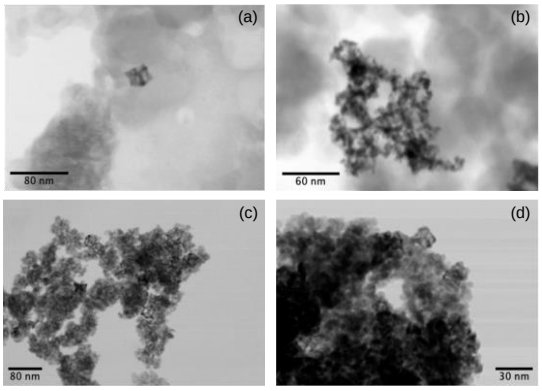

Figure 7. STEM images after ADT of 10,000 cycles showing (a-b) PtNiIr NF/C and (c-d) PtNiIr NF/ATO samples.

From these results, there is a noticeable difference in the effect of supports when interacting with PtNiIr NFs. Studies examining SMSIs have noted the proclivity of reducible oxides (Ti, Fe, Sn etc.) to reduce and encapsulate metal catalysts in surface oxygen.[54-58] The coverage by oxygen could hinder the mobility or migration of catalysts as observed in STEM following 10,000 cycles of ADT.[57] In addition, encapsulation is predicted only for metals with surface energies in excess of 2 J/m^2, where Pt(111) and Ir(111) surface energies are 2.30 and 2.97, respectively.[59] Suppression of CO adsorption seen in $ECSA_{CO}$ values also provides evidence of encapsulation of NFs (PtNiIr NF/ATO (71.2 $m^2\ g_{Pt}^{-1}$) and PtNiIr NF/C (48.6 $m^2\ g_{Pt}^{-1}$)).[57] Encapsulation of catalysts is also an indication of SMSIs which were observed in XPS data.[50] Finally, XANES measurements indicates that surface iridium, present in the structural extremities, has been oxidized to a greater extent than when supported on carbon. The encapsulation of NFs, either fully or partially, would help explain the improved performance and durability observed in PtNiIr NF/ATO samples.

4. Conclusions

Support effects on the durability and OER performance of PtNiIr rhombic dodecahedral NFs were examined in this study. Examining these NFs in STEM revealed the presence of iridium at the edges and vertices of the NFs while also confirming the formation of a (Pt,Ir) alloy in these regions. Different loading methods were compared for the optimal loading on PtNiIr NF/ATO. Use of $BuNH_2$ likely remove excess oleylamine and then improved the SMSI between PtNiIr NFs and ATO. Comparing PtNiIr NFs to PtNi NFs indicated that the presence of iridium drastically improves OER performance regardless of support.

XPS characterization indicated strong metal support interactions (SMSI) in agreement with previous studies into platinum and iridium-based catalysts loaded onto metal supports. PtNiIr NF/ATO samples showed a turnover frequency of 0.30 s^{-1} and a Faradaic efficiency of 92% which were calculated from O_2 generated in an OLEMS setup. These values are almost the same as PtNiIr NF/C samples, indicating that ATO provides a stable support with a comparable amount of charge transfer with loaded NFs.

Extended ADT illustrates the effects of carbon corrosion on the overall OER performance whereas ATO loaded samples maintained a similar mass activity after 10,000 cycles. STEM confirmed that these samples showed no signs of NFs migration, dissolution or agglomeration when compared to carbon. Finally, XANES measurements of samples following electrochemical cleaning/activation indicated a lower oxidation state of iridium on metal oxide loaded samples. From our findings, the combination of ATO and PtNiIr NFs shows promise as an integrated catalytic system in water oxidation applications.

ASSOCIATED CONTENT

Supporting Information

The Supporting Information is available free of charge on the ACS Publications website.
Calibration curve and OLEMS results; STEM images of PtNiIr NFs; LSVs of PtNi and PtNiIr NFs with different synthesis and loading methods; CO stripping voltammograms of PtNiIr NF/C and PtNiIr NF/ATO; O_2 calibration curve and OLEMS results; and ICP-MS measurements of PtNiIr NF/ATO samples before and after ADT (10,000 cycles) (PDF)

AUTHOR INFORMATION

Corresponding Author

*Email: colin.tadgell@ees.hokudai.ac.jp (CT); masaru.kato@ees.hokudai.ac.jp (MK); iyagi@ees.hokudai.ac.jp (IY).

Author Contributions

C.A.T. carried out the synthesis, characterization, and electrocatalysis. M.K., K.M. and I.Y. supervised the project. M.K. and I.Y. conceptualized the project. The manuscript was written through contributions of all authors. All authors wrote, commented on and approved the final version of the manuscript.

Notes

The authors declare no competing financial interest.

ACKNOWLEDGMENT

The authors thank Naomi Hirai (Research Institute for Electronic Science, Hokkaido University) for taking the HAADF–STEM and EDS mapping images. X-ray absorption spectroscopy was performed at the beamline BL12C, Photon Factory, KEK (proposal no. 2021G083). This work was supported by the Japan Society for the Promotion of Science (JSPS) (20F19756) and the Nanotechnology Platform program of the Ministry of Education, Culture, Sports, Science and Technology (MEXT) for Hokkaido University (JPMXP09A17HK0073, 18HK0063, 19HK0030 and 21HK0062).

REFERENCES

1. Carmo, M.; Fritz, D.L.; Mergel, J.; Stolten, D., A Comprehensive Review on PEM Water Electrolysis. *Int. J. Hydrogen Energy* **2013**, 38.12, 4901-4934, DOI: 10.1016/j.ijhydene.2013.01.151
2. Oh, H.S.; Nong, H.N.; Reier, T.; Gliech, M.; Strasser, P., Oxide-supported Ir nanodendrites with high activity and durability for the oxygen evolution reaction in acid PEM water electrolyzers. *Chem. Sci.* **2015**, *6*(6), pp.3321-3328. DOI: 10.1039/c5sc00518c

3. Wang, C.; Li, D.; Chi, M.; Pearson, J.; Rankin, R.B., Greeley; J., Duan, Z.; Wang, G.; Van der Vliet, D.; More, K.L.; Markovic, N.M., Rational development of ternary alloy electrocatalysts. *J. Phy. Chem. Lett.* **2012**, *3*(12), pp.1668-1673. DOI: 10.1021/jz300563z
4. Kim, J.; Choi, H.; Kim, D.; Park, J.Y., Operando surface studies on metal-oxide interfaces of bimetal and mixed catalysts. *ACS Catal.* **2021**, *11*(14), pp.8645-8677. DOI: 10.1021/acscatal.1c02340
5. Chen, C.; Kang, Y.; Huo, Z.; Zhu, Z.; Huang, W.; Xin, H.L.; Snyder, J.D.; Li, D.; Herron, J.A.; Mavrikakis, M.; Chi, M., Highly Crystalline Multimetallic Nanoframes with Three-Dimensional Electrocatalytic Surfaces. *Science* **2014**, 343, 1339-1343, DOI: 10.1126/science.1249061.
6. Kwon, T.; Jun, M.; Lee, K., Catalytic nanoframes and beyond. *Adv. Mater.* **2020**, *32*(33), p.2001345. DOI: 10.1002/adma.202001345
7. Kato, M.; Ogura, K.; Nakagawa, S.; Tokuda, S.; Takahashi, K.; Nakamura, T.; Yagi, I., Enhancement of Electrocatalytic Oxygen Reduction Activity and Durability of Pt–Ni Rhombic Dodecahedral Nanoframes by Anchoring to Nitrogen-Doped Carbon Support. *ACS Omega* **2018**, 3, 9052-9059, DOI: 10.1021/acsomega.8b01373.
8. Kato, M.; Nakahoshiba, R.; Ogura, K.; Tokuda, S.; Yasuda, S.; Higashi, K.; Uruga, T.; Uemura, Y.; Yagi, I., Electronic Effects of Nitrogen Atoms of Supports on Pt–Ni Rhombic Dodecahedral Nanoframes for Oxygen Reduction. *ACS App. Energy Mater.* **2020**, 3(7), pp.6768-6774. DOI: 10.1021/acsaem.0c00903
9. Xia, Y.; Xiong, Y.; Lim, B.; Skrabalak, S.E., Shape-controlled synthesis of metal nanocrystals: simple chemistry meets complex physics? *Angew. Chem. Int. Ed.* **2009**, *48*(1), pp.60-103. DOI: 10.1002/anie.200802248
10. Gruzeł, G.; Szmuc, K.; Drzymała, E.; Piekarz, P.; Pajor-Świerzy, A.; Budziak, A.; Pastor, E., Thin layer vs. nanoparticles: Effect of SnO_2 addition to PtRhNi nanoframes for ethanol oxidation reaction. *Int. J. Hydrogen Energy* **2022**, *47*(33), pp.14823-14835. DOI: 10.1016/j.ijhydene.2022.02.217
11. Wang, Z.; Huang, L.; Tian, Z.Q.; Shen, P.K., The controllable growth of PtCuRh rhombic dodecahedral nanoframes as efficient catalysts for alcohol electrochemical oxidation. *J. Mater. Chem. A* **2019**, *7*(31), pp.18619-18625. DOI: 10.1039/C9TA06119C
12. Pi, Y.; Shao, Q.; Zhu, X.; Huang, X., Dynamic structure evolution of composition segregated iridium-nickel rhombic dodecahedra toward efficient oxygen evolution electrocatalysis. *ACS Nano* **2018**, *12*(7), pp.7371-7379. DOI: 10.1021/acsnano.8b04023
13. Young, J.L.; Kang, Z.; Ganci, F.; Madachy, S; Bender, G., PEM electrolyzer characterization with carbon-based hardware and material sets. *Electrochem. Commun.* **2021**, 124, p.106941. DOI: 10.1016/j.elecom.2021.106941
14. Pantò, F.; Siracusano, S.; Briguglio, N.; Aricò, A.S., Durability of a recombination catalyst-based membrane-electrode assembly for electrolysis operation at high current density. *App. Energy* **2020**, 279, p.115809. DOI: 10.1016/j.apenergy.2020.115809
15. Siracusano, S.; Trocino, S.; Briguglio, N.; Pantò, F.; Aricò, A.S., Analysis of performance degradation during steady-state and load-thermal cycles of proton exchange membrane water electrolysis cells. *J. Power Sources* **2020**, 468, p.228390. DOI: 10.1016/j.jpowsour.2020.228390
16. Siracusano, S.; Baglio, V.; D'Urso, C.; Antonucci, V.; Aricò, A.S., Preparation and characterization of titanium suboxides as conductive supports of IrO2 electrocatalysts for application in SPE electrolysers. *Electrochim. Acta* **2009**, *54*(26), pp.6292-6299. DOI: 10.1016/j.electacta.2009.05.094
17. Puthiyapura, V.K.; Pasupathi, S.; Basu, S.; Wu, X.; Su, H.; Varagunapandiyan, N.; Pollet, B.; Scott, K., $RuxNb_{1-x}O_2$ catalyst for the oxygen evolution reaction in proton exchange membrane water electrolysers. *Int. J. Hydrogen Energy* **2013**, *38*(21), pp.8605-8616. DOI: 10.1016/j.ijhydene.2013.04.100
18. Ferro, S.; Rosestolato, D.; Martínez-Huitle, C.A.; De Battisti, A., On the oxygen evolution reaction at IrO_2-SnO_2 mixed-oxide electrodes. *Electrochim. Acta* **2014**, *146*, pp.257-261. DOI: 10.1016/j.electacta.2014.08.110
19. Polonský, J.; Petrushina, I.M.; Christensen, E.; Bouzek, K.; Prag, C.B.; Andersen, J.E.T.; Bjerrum, N.J., Tantalum carbide as a novel support material for anode electrocatalysts in polymer electrolyte membrane water electrolysers. *Int. J. Hydrogen Energy* **2012**, *37*(3), pp.2173-2181. DOI: 10.1016/j.ijhydene.2011.11.035
20. Karimi, F.; Peppley, B.A., Metal carbide and oxide supports for iridium-based oxygen evolution reaction electrocatalysts for polymer-electrolyte-membrane water electrolysis. *Electrochim. Acta* **2017**, *246*, pp.654-670. DOI: 10.1016/j.electacta.2017.06.048
21. Oh, H.S.; Nong, H.N.; Strasser, P., Preparation of mesoporous Sb-, F-, and In-doped SnO_2 bulk powder with high surface area for use as catalyst supports in electrolytic cells. *Adv. Funct. Mater.* **2015**, *25*(7), pp.1074-1081. DOI: 10.1002/adfm.201401919
22. Mohanta, P.K.; Glökler, C.; Arenas, A.O.; Jörissen, L., Sb doped SnO2 as a stable cathode catalyst support for low temperature polymer electrolyte membrane fuel cell. *Int. J. Hydrogen Energy* **2017**, *42*(46), pp.27950-27961. DOI: 10.1016/j.ijhydene.2017.06.064
23. Jang, H.; Lee, J.H.; Lee, J.R.; Kim, T.W., Metal–Support Interaction Can Deactivate IrO_x/Sb: SnO_2 OER Catalysts in Polyol Process. *ACS Appl. Energy Mater.* **2022**, *5*(8), pp.9297-9302. DOI: 10.1021/acsaem.2c01765
24. Hartig-Weiss, A.; Miller, M.; Beyer, H.; Schmitt, A.; Siebel, A.; Freiberg, A.T.; Gasteiger, H.A.; El-Sayed, H.A., Iridium Oxide Catalyst Supported on Antimony-Doped Tin Oxide for High Oxygen Evolution Reaction Activity in Acidic Media. *ACS Appl. Nano Mater.* **2020** 3.3, 2185-2196, DOI: 10.1021/acsanm.9b02230
25. Bruix, A.; Rodriguez, J.A.; Ramírez, P.J.; Senanayake, S.D.; Evans, J.; Park, J.B.; Stacchiola, D.; Liu, P.; Hrbek, J.; Illas, F., "A new type of strong metal–support interaction and the production of H_2 through the transformation of water on Pt/CeO_2 (111) and Pt/CeO_x/TiO_2 (110) catalysts." *J. Am. Chem. Soc.* **2012,** 134.21, 8968-8974. DOI: 10.1021/ja302070k
26. Saveleva, V.A.; Wang, L.; Kasian, O.; Batuk, M., Hadermann, J.; Gallet, J.J.; Bournel, F.; Alonso-Vante, N.; Ozouf, G.; Beauger, C.; Mayrhofer, K.J.J., Insight into the mechanisms of high activity and stability of iridium supported on antimony-doped tin oxide aerogel for anodes of proton exchange membrane water electrolyzers. *ACS Catal.* **2020**, 10(4), pp.2508-2516. DOI: 10.1021/acscatal.9b04449
27. Choi, S.; Park, J.; Kabiraz, M.K.; Hong, Y.; Kwon, T.; Kim, T.; Oh, A.; Baik, H.; Lee, M.; Paek, S.M.; Choi, S.I.; Lee, K., Pt Dopant: Controlling the Ir Oxidation States Toward Efficient and Durable Oxygen Evolution Reaction in Acidic Media. *Adv. Funct. Mater.* **2020**, 30.38, 2003935, DOI: 10.1002/adfm.202003935
28. Reier, T.; Nong, H.N.; Teschner, D.; Schlögl, R.; Strasser, P., Electrocatalytic Oxygen Evolution Reaction in Acidic Environments–Reaction Mechanisms and Catalysts. *Adv. Energy Mater.* **2017**, 7.1, 1601275, DOI: 10.1002/aenm.201601275

29. Kato, M.; Unuma, Y.; Okui, M.; Qu, Y.; Zheng, J.; Taguchi, S.; Kiguchi, F.; Torihata, M.; Gao, Y.; Hoshi, N.; Yagi, I., Electrocatalytic activity and volatile product selectivity for nitrate reduction at tin-modified Pt (100), Pd (100) and Pd–Pt (100) single crystal electrodes in acidic media. *Electrochim. Acta* **2021**, *398*, p.139281. DOI: 10.1016/j.electacta.2021.139281
30. Qu, Y.; Wang, L.; Li, C.; Gao, Y.; Sik, J.K.; Rao, J.; Yin, G., Quantitative pinhole on-line electrochemical mass spectrometry study on ethanol electro-oxidation at carbon-supported Pt and Ir-containing catalysts. *Int. J. of Hydrogen Energy* **2017**, *42*(1), pp.228-235. DOI: 10.1016/j.ijhydene.2016.08.215
31. Görlin, M.; Chernev, P.; Ferreira de Araújo, J.; Reier, T.; Dresp, S.; Paul, B.; Krähnert, R.; Dau, H.; Strasser, P., Oxygen evolution reaction dynamics, faradaic charge efficiency, and the active metal redox states of Ni–Fe oxide water splitting electrocatalysts. *J. Am. Chem. Soc.* **2016**, *138*(17), pp.5603-5614. DOI: 10.1021/jacs.6b00332
32. Geiger S.; Kasian O.; Ledendecker M.; Pizzutilo E.; Mingers AM.; Fu WT.; Diaz-Morales O.; Li Z.; Oellers T.; Fruchter L.; Ludwig A., The Stability Number as a Metric for Electrocatalyst Stability Benchmarking." *Nat. Catal.* **2018**, 1.7, 508-515, DOI: 10.1038/s41929-018-0085-6
33. Kato, M.; Kimijima, K.I.; Shibata, M.; Notsu, H.; Ogino, K.; Inokuma, K.; Ohta, N.; Uehara, H.; Uemura, Y.; Oyaizu, N.; Ohba, T., Deprotonation of a dinuclear copper complex of 3, 5-diamino-1, 2, 4-triazole for high oxygen reduction activity. PCCP **2015**, 17(14), pp.8638-8641. DOI: 10.1039/C4CP05595K
34. Ravel, B.; Newville, M.A.T.H.E.N.A., ATHENA, ARTEMIS, HEPHAESTUS: data analysis for X-ray absorption spectroscopy using IFEFFIT. *J. Synchrotron Radiat.* **2005**, *12*(4), pp.537-541. DOI: 10.1107/S0909049505012719
35. Karimi, F.; Peppley, B.A., Metal Carbide and Oxide Supports for Iridium-Based Oxygen Evolution Reaction Electrocatalysts for Polymer-Electrolyte-Membrane Water Electrolysis. *Electrochim. Acta* **2017**, 246, 654-670, DOI: 10.1016/j.electacta.2017.06.048
36. Oh, H.S.; Nong, H.N.; Reier, T.; Bergmann, A.; Gliech, M.; Ferreira de Araújo, J.; Willinger, E.; Schlögl, R.; Teschner, D.; Strasser, P., Electrochemical Catalyst–Support Effects and Their Stabilizing Role for IrO_x Nanoparticle Catalysts During the Oxygen Evolution Reaction. *J. Am. Chem. Soc.* **2016**, 138.38, 12552-12563, DOI: 10.1021/jacs.6b07199
37. Chen, S.; Niu, Z.; Xie, C.; Gao, M.; Lai, M.; Li, M.; Yang, P., Effects of catalyst processing on the activity and stability of Pt–Ni nanoframe electrocatalysts. ACS nano **2018**, 12(8), pp.8697-8705. DOI: 10.1021/acsnano.8b04674
38. Wu, J.; Zhang, J.; Peng, Z.; Yang, S.; Wagner, F.; Yang, H., Truncated octahedral Pt_3Ni oxygen reduction reaction electrocatalysts. *J. Am. Chem. Soc.* **2010**, 132.14, 4984-4985, DOI: 10.1021/ja100571h
39. Zhiqiang, N.; Li, Y., Removal and utilization of capping agents in nanocatalysis. *Chem. Mater.* **2014**, 26.1, 72-83, DOI: 10.1021/cm4022479
40. Miyabayashi, K.; Shirayama, Y.; Surabhi, G; Tatsuoka, H., Identical-location Transmission Electron Microscopy of Pt Nanoparticle Electrocatalysts Using Iridium-coated Au Grids for Fuel Cell Durability Tests Simulating Start-up and Shutdown Conditions. Electroanalysis **2023**, 35(4), 202200199, DOI: 10.1002/elan.202200199
41. Wu, J.; Yang, S.; Yang, H., Facet-controlled metal alloy electrocatalysts for oxygen reduction reaction: unconventional post treatment of Pt_3Ni octahedral catalysts for enhanced activity. ECS Trans. **2014**, 61(31), p.25., DOI: 10.1149/06131.0025ecst
42. You, H.; Wang, W.; Yang, S., A universal rule for organic ligand exchange. ACS Appl. Mater. Interfaces **2014**, 6(21), pp.19035-19040. DOI: 10.1021/am504918z
43. Arán-Ais, R.M.; Vidal-Iglesias, F.J.; Solla-Gullón, J.; Herrero, E.; Feliu, J.M., Electrochemical characterization of clean shape-controlled Pt nanoparticles prepared in presence of oleylamine/oleic acid. Electroanalysis **2015**, 27(4), pp.945-956, DOI: 10.1002/elan.201400619
44. Goebbert, C.; Nonninger, R.; Aegerter, M.A.; Schmidt, H., Wet chemical deposition of ATO and ITO coatings using crystalline nanoparticles redispersable in solutions. Thin solid films **1999**, 351(1-2), pp.79-84, DOI: 10.1016/S0040-6090(99)00209-6
45. Pi, Y., Xu, Y., Li, L., Sun, T., Huang, B., Bu, L., Ma, Y., Hu, Z., Pao, C.W. and Huang, X., Selective Surface Reconstruction of a Defective Iridium‐Based Catalyst for High‐Efficiency Water Splitting. *Adv. Funct. Mater.* **2020**, 30(43), p.2004375. DOI: 10.1002/adfm.202004375
46. Nong, H.N.; Reier, T.; Oh, H.S.; Gliech, M.; Paciok, P.; Vu, T.H.T.; Teschner, D.; Heggen, M.; Petkov, V.; Schlögl, R.; Jones, T., A unique oxygen ligand environment facilitates water oxidation in hole-doped $IrNiO_x$ core–shell electrocatalysts. *Nat. Catal.* **2018**, *1*(11), pp.841-851. DOI: 10.1038/s41929-018-0153-y
47. Godínez-Salomón, F.; Albiter, L.; Alia, S.M.; Pivovar, B.S.; Camacho-Forero, L.E.; Balbuena, P.B.; Mendoza-Cruz, R.; Arellano-Jimenez, M.J.; Rhodes, C.P., Self-supported hydrous iridium–nickel oxide two-dimensional nanoframes for high activity oxygen evolution electrocatalysts. *ACS Catal.* **2018**, *8*(11), pp.10498-10520. DOI: 10.1021/acscatal.8b02171
48. Tahir, M.; Pan, L.; Idrees, F.; Zhang, X.; Wang, L.; Zou, J.J.; Wang, Z.L., Electrocatalytic Oxygen Evolution Reaction for Energy Conversion and Storage: A Comprehensive Review. *Nano Energy* **2017**, 37, 136-157, DOI: 10.1016/j.nanoen.2017.05.022
49. Courtois, J., Du, W., Wong, E., Teng, X. and Deskins, N.A. Screening iridium-based bimetallic alloys as catalysts for direct ethanol fuel cells. *Appl. Catal. A: Gen.***2014**, 483, pp.85-96. DOI: 10.1016/j.apcata.2014.06.029
50. Lewera, A.; Timperman, L.; Roguska, A.; Alonso-Vante, N., Metal–support interactions between nanosized Pt and metal oxides (WO_3 and TiO_2) studied using X-ray photoelectron spectroscopy. *J. Phy. Chem. C* **2011**, *115*(41), pp.20153-20159. DOI: 10.1021/jp2068446
51. Rajan, Z.S.; Binninger, T.; Kooyman, P.J.; Susac, D.; Mohamed, R., Organometallic chemical deposition of crystalline iridium oxide nanoparticles on antimony-doped tin oxide support with high-performance for the oxygen evolution reaction. *Catal. Sci. Technol.* **2020**, *10*(12), pp.3938-3948. DOI: 10.1039/d0cy00470g
52. He, C.; Sankarasubramanian, S.; Ells, A.; Parrondo, J.; Gumeci, C.; Kodali, M.; Matanovic, I.; Yadav, A.K.; Bhattacharyya, K.; Dale, N.; Atanassov, P., Self-anchored platinum-decorated antimony-doped-tin oxide as a durable oxygen reduction electrocatalyst. *ACS Catal* **2021** 11.12, 7006-7017. DOI: 10.1021/acscatal.1c00963
53. Durante, C., "Metal–Carbon Interaction in metal Nanoparticles and implication in the Electrocatalysis of Oxygen Reduction." *Curr. Opin. Electrochem.* **2022**, 101119, DOI: 10.1016/j.coelec.2022.101119
54. Bonanni, S.; Aït-Mansour, K.; Brune, H.; Harbich, W., Overcoming the strong metal– support interaction state: CO oxidation on TiO_2 (110)-supported Pt nanoclusters. *ACS Catal.* **2011**, 1(4), pp.385-389. DOI: 10.1021/cs200001y
55. Qin, Z.H.; Lewandowski, M.; Sun, Y.N.; Shaikhutdinov, S.; Freund, H.J., Encapsulation of Pt nanoparticles as a result of strong metal– support interaction with Fe_3O_4

(111). *The J. Phys. Chem. C* **2008**, 112(27), pp.10209-10213. DOI: 10.1021/jp801756q
56. Kamiuchi, N.; Muroyama, H.; Matsui, T.; Kikuchi, R.; Eguchi, K., Nano-structural changes of SnO_2-supported palladium catalysts by redox treatments. *Appl. Catal. A-Gen* **2010**, 379(1-2), pp.148-154. DOI: 10.1016/j.apcata.2010.03.019
57. Han, B.; Guo, Y.; Huang, Y.; Xi, W.; Xu, J.; Luo, J.; Qi, H.; Ren, Y.; Liu, X.; Qiao, B.; Zhang, T., Strong metal–support interactions between Pt single atoms and TiO_2. *Angew. Chem. Int. Ed.* **2020**, 59(29), pp.11824-11829. DOI: 10.1002/anie.202003208
58. Tang, M.; Li, S.; Chen, S.; Ou, Y.; Hiroaki, M.; Yuan, W.; Zhu, B.; Yang, H.; Gao, Y.; Zhang, Z.; Wang, Y., Facet‐Dependent Oxidative Strong Metal‐Support Interactions of Palladium‐TiO_2 Determined by In Situ Transmission Electron Microscopy. *Angew. Chem. Int. Ed.* **2021**, 60(41), pp.22339-22344. DOI: 10.1002/anie.202106805
59. Fu, Q.; Wagner, T., Interaction of nanostructured metal overlayers with oxide surfaces. *Surf. Sci. Rep.* **2007**, 62(11), pp.431-498. DOI: 10.1016/j.surfrep.2007.07.001
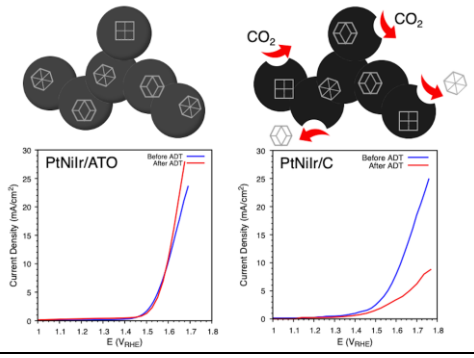
SYNOPSIS TOC